Composites Part B 283 (2024) 111584

Contents lists available at ScienceDirect

Composites Part B

journal homepage: www.elsevier.com/locate/composites

Failsafe layer for wind turbine blades: Erosion protection of glass fiber composite through nanodiamond-treated flax composite top layer

Carsten Hinzmann [a,*], Nicolai Frost-Jensen Johansen [b], Charlotte Bay Hasager [b], Bodil Holst [a]

[a] Department of Physics and Technology, University of Bergen, Allégaten 55, Bergen, 5033, Norway
[b] Department of Wind and Energy Systems, Technical University of Denmark, RisøCampus, Frederiksborgvej 399, Roskilde, 4000, Denmark

ARTICLE INFO

Keywords:
A. Natural fiber
A. Nanoparticles
B. Impact behavior
D. Acoustic emission

ABSTRACT

Wind turbine blades are mainly made from E-glass fiber (GF) epoxy composites, because of their good ratio of strength to weight and costs. With the increase in blade length and tip speed, the problem of leading edge erosion is becoming more severe, reducing annual energy production and raising maintenance cost. It was recently shown that nanodiamond-treated flax fiber (FF_{ND}) composites have significantly less erosion than GF composites and could be an alternative for GF in the turbine blade aeroshells. However, FF_{ND} alone might not be suitable for manufacturing turbine blades at the large scale of modern wind turbines. Here, we show that a hybrid composite with a thin layer of only 1.5 mm of FF_{ND} on a GF base, can achieve the same superior results as bulk material FF_{ND} composite. In addition, we show and explain why aramid fibers, that are known for impact resistance, do not perform well as erosion protection. Our research shows the great potential of this technology to be implemented as a low-cost, lightweight skin layer on the leading edge. Acting as damage-tolerant failsafe layer, negligible ~ 0.04 % extra weight of the FF_{ND} could increase the blade's base erosion resistance by a factor of 60±20 compared to plain GF, expanding the repair window, reducing costs, and enhancing reliability.

1. Introduction

Wind turbine blades are mainly made from type E glass fiber (GF) epoxy composites, because of their good combination of properties (moderate stiffness, high strength, moderate density) and cost effective production [1].

With the increase in blade length and tip speed [2], leading edge erosion is becoming a severe problem for the wind energy industry, reducing annual energy production [3,4] and raising maintenance cost [5]. New base materials for wind turbine blades with less impact fatigue and more erosion resistance are of great interest, since each leading edge protection has a finite life time [6–8].

Aramid fibers (AFs) are known for their high thermal stability, chemical and impact resistance [9,10], which is exploited in antiballistic, protective applications [10,11]. AFs have a higher tensile strength and higher elastic modulus than GFs [1], and have a higher toughness [12] and lower density than carbon fibers (CFs) [1]. In contrast to CFs, AFs are electrical insulating [9] and therefore suitable as material for wind turbine blade aeroshells, without compromising lightning protection. Together, this makes AFs to a promising material for erosion impact protection.

In a previous study, we showed that natural flax fiber (FF) and nanodiamond-treated flax fiber (FF_{ND}) composites have significantly less erosion than GF composites, tested in the single point impact fatigue test (SPIFT) [13]. The performance gap was explained with different properties of the fibers that led to lower impact pressure, less stress wave reflections and better impact energy absorption of the FFs [13]. However, this needs to be verified with additional measurements.

The aspect of sustainability and competitive specific mechanical properties makes FFs to an attractive substitute for GFs in composites [14,15]. This is enhanced by the treatment of flax with nanodiamonds, that improve the fiber's performance [13,16], without making them to a health or environment hazard [17].

Even though it has been shown that FFs are a suitable structural replacement to GFs in small wind turbine blades of 3.5 m length (i.e. for 11 kW turbine) [18], flax alone might not be suitable for manufacturing turbine blades of over 100 m length (i.e. for 15 MW offshore turbine [19]). Beside its lower mechanical performance, flax has a different failure behavior with varying stress–strain accumulation mechanisms. Both could be potentially overcome with new design solutions, but this requires extensive and cost intensive testing of large structures [18].

* Corresponding author.
E-mail address: carsten.hinzmann@posteo.net (C. Hinzmann).

https://doi.org/10.1016/j.compositesb.2024.111584
Received 25 February 2024; Received in revised form 21 May 2024; Accepted 22 May 2024
Available online 23 May 2024

Hybrid composites for the aeroshells could be an inexpensive solution for combining conventional blade designs with erosion resistant materials. This has been proposed as protection against sand erosion with CF leading edges [20].

In this work we present an investigation of the erosion properties of three different hybrid composites, with a top layer of flax (i), nanodiamond-treated flax (ii) and aramid (iii) fibers, all with a base layer of GFs. In addition to measurements of impact fatigue and mass loss, the acoustic emissions of the impacts were recorded, in order to receive more information about the impact energy absorption. The flax fiber hybrid (H-FF), nanodiamond-treated flax fiber hybrid (H-FF_{ND}) and aramid fiber hybrid (H-AF) reinforced epoxy composites are compared to standard bulk GF, FF and FF_{ND} reinforced epoxy composites, reported in [13].

2. Material and methods

2.1. Materials

Flax fabric with 2/2-twill weave pattern, made from twisted yarns, was chosen because of its beneficial damping [21] and impact fatigue properties in composites [13]. It had a fabric weight of $(136 \pm 2)\,g\,m^{-2}$ and was supplied by Libeco NV, Belgium. The yarns had a number metric of 36 N m and twist level of 670 tpm, which corresponds to a surface twist angle of about 21° according to Shah et al. [22]. A nanodiamond-water-dispersion (uDiamond® Hydrogen D) of hydrogen-terminated nanodiamonds was supplied by Carbodeon Ltd Oy, Finland and had a concentration of 2.5 wt %.

Standard bi-axial grade E GF fabric of $(600 \pm 3)\,g\,m^{-2}$, 2/2-twill grade E GF fabric of $(204 \pm 3)\,g\,m^{-2}$ and DuPont Kevlar 49, AF fabric of $(317 \pm 2)\,g\,m^{-2}$ were supplied by Easy Composites Ltd, United Kingdom, as well as the epoxy resin system, EC-IN2 infusion resin with EC-AT30-SLOW hardener.

2.2. Nanodiamond treatment of flax

The nanodiamond treatment was performed as described in [13]. The size of the flax fabric was 260 mm × 450 mm and the fabric was mounted on a sample holder, clamping all fiber ends. The concentration of the nanodiamond dispersion was reduced from 2.5% to 0.3% with deionized water. The cleaning and treatment of the fabric was performed with a Sonomatic 3800, Langford Electronics Ltd., United Kingdom, ultrasonic cleaner, working at a frequency of 33 kHz with 600 W ultrasonic power. First, the flax fabric was cleaned with isopropanol for 3 min and then with deionized water for 20 min using ultrasonic agitation. The treatment with nanodiamonds was performed directly after cleaning without drying the fabric in between. The flax was dip-coated in the nanodiamond dispersion for 30 min using ultrasonic agitation and rinsed with deionized water thereafter. Lastly, the treated flax was dried on a hotplate at 60 °C for at least 6 h to evaporate water without degrading the flax [23].

2.3. Experimental design and composite fabrication

The composites studied in this work were hybrid composites, consisting of two different reinforcement materials. By using a common base material (GF) the variation in stiffness between samples is minimized resulting in more comparable results. Bi-axial GF formed a base layer for all samples, emulating the base material of wind turbine blades, and 2/2-twill weaves of FF, FF_{ND} and AF formed a thinner top layer as shown in Fig. 1. These hybrid samples were compared to pure GF samples with 2/2-twill GF as top layer.

Following the approach of [13], we aimed for equal composite thicknesses with a combined thickness of base and top layer of more than 5 mm in order to achieve optimal comparability to bulk FF and FF_{ND} material samples previously investigated [13]. The top layer of the hybrid composites was designed to be of equal thickness for all types of reinforcements with the minimal number of fabric plies possible. This was achieved by interpolating the needed number of plies of each material from test composites.

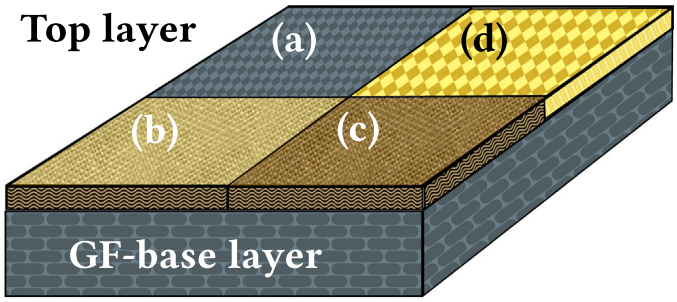

Fig. 1. Sketch of hybrid composite sample with a bi-axial GF base layer and different top layers of 2/2-twill GF (a), FF (b), FF_{ND} (c) and AF (d); The drawing emphasizes that all top layers were impregnated together with the same GF base in a single vacuum-assisted resin infusion.

The layup of the composites consisted of nine plies of $(600 \pm 3)\,g\,m^{-2}$ bi-axial GF fabric and formed the same base layer for all samples. Each reinforcement material had a section of about 90 mm × 90 mm size on top of the base layer to form the different top layers of the samples as shown in Fig. 1. The samples were impregnated together in a single vacuum-assisted resin infusion, in order to achieve an equal ratio of fiber and resin in the base layer of all samples. After curing for 24 h at room temperature, the composite was post-cured in an oven before demoulding with the following curing cycle: 2 h at 40 °C, 2 h at 50 °C and 5 h at 60 °C. Table 1 shows a summary of fabrication steps and the layup, including the ply numbers of the top layers. Before performing the SPIFT, the different composite were cut into samples of about 40 mm × 40 mm.

2.4. Fiber volume fraction and areal porosity

In composites the fiber volume fraction is a fundamental characteristic for the material's mechanical performance. The composite volume (V_c) consists of the volume of fibers (V_f), matrix (V_m) and voids (V_p) and their volume fractions ($VF = V/V_c$) sum to one [24]:

$$V_c = V_f + V_m + V_p \tag{1a}$$

$$\Rightarrow 1 = VF_f + VF_m + VF_p \tag{1b}$$

The volumetric composition of the top and base layer differs for hybrid composites because of the different fiber reinforcements. Therefore, it is not possible to measure the volumetric composition of the hybrid composites with the buoyancy method. However, knowing the thickness of each layer (t_l) as well as the fiber density (ρ_f), the fabric weight ($\rho_{A,f}$) and the number of plies (N), the fiber volume fraction (VF_f) of the top and base layer can be estimated by

$$VF_f = \frac{V_f}{V_l} = \frac{N \cdot \rho_{A,f}}{\rho_f \cdot t_l} \tag{2}$$

with V_f being the fiber volume and V_l the layer volume. In order to calculate VF_f, the fiber densities were taken from previous publications. Rude et al. [25] measured the density of GF as $(2.617 \pm 0.005)\,g\,cm^{-3}$, Mehmood and Madsen [26] measured the density of FF as $(1.59 \pm 0.05)\,g\,cm^{-3}$ and DuPont [27] states the density of AF as $1.44\,g\,cm^{-3}$. The layer thicknesses were measured with calipers, having an uncertainty of 0.05 mm.

The areal porosity (A_p) was measured as described in [13] with the area fraction of voids in sample cross section images. The single voids were approximated as spheres. Their total area is the sum of the single

Table 1
Composite layup and fabrication.

		GF	H-FF	H-FF$_{ND}$	H-AF
Top layer	Fabric type	2/2-twill woven fabric			
	Fabric weight [g/m^2]	204 ± 3	136 ± 2	136 ± 2	317 ± 2
	Ply number	7	4	4	3
Base layer	Fabric type	Bi-axial GF			
	Fabric weight [g/m^2]	600 ± 3			
	Ply number	9			
	Epoxy resin system	EC-IN2 infusion resin with EC-AT30-SLOW hardener			
	Impregnation process	Vacuum-assisted resin infusion			
	Curing cycle	24 h at room temperature, 2 h at 40 °C, 2 h at 50 °C and 5 h at 60 °C			

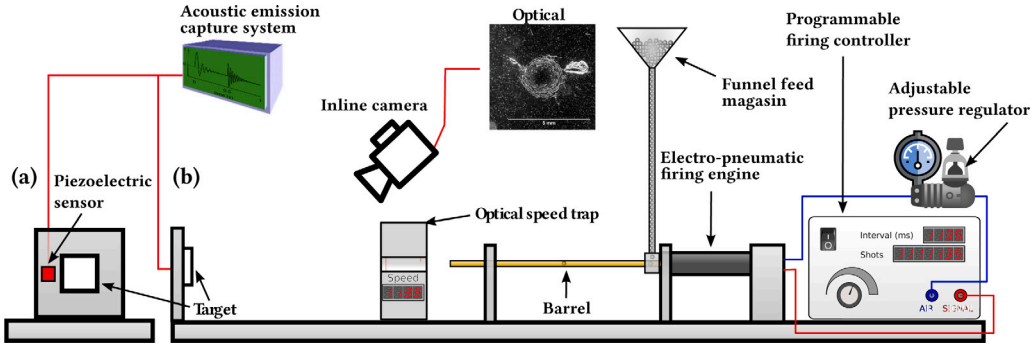

Fig. 2. Illustration of the SPIFT, with instrumentation and control systems; (a) Front view of sample holder with piezoelectric sensor mounted next to the target, measuring the acoustic emission of each impact; (b) Side view of testing setup; Compressed air accelerates the rubber balls through the barrel; An optical speed trap is placed 200 mm in front of the sample holder and records the rubber ball's velocity before it hits the target; A camera monitors and records the sample surface during the entire test. More details can be found in the main text and in [28,29].

inclusion areas A_i with radius r_i, such that the areal porosity is given by

$$A_p = \frac{\sum_i^N A_i}{A_s}, \text{ with } A_i = r_i^2 \pi \tag{3}$$

with A_s being the area of the image section.

2.5. Single point impact fatigue test (SPIFT), mass loss and acoustic emission

The SPIFT was used to study the impact fatigue behavior of the composite samples and to monitor the damage progression at a single impact point. It was performed with an electro-pneumatic projectile firing device, for a detailed description see [28,29]. Fig. 2 shows the SPIFT setup used in this work with an optical camera and an acoustic emission capture system. The projectiles used are nitrile rubber balls with an average mass and density of (143 ± 3) mg and (1.09 ± 0.02) g cm^{-3}, respectively [13]. Via a vibratory feed system the projectiles are fed to the pneumatic firing engine (Valken V12), compressed air accelerates them through the barrel and shoots them on the target. The impact velocity (v_{impact}) is controlled by adjusting the air pressure and measured by an optical speed trap (AirChrony MkIII). The impact rate and maximum impact number is set via the controller, initiating the test.

The sample surface is monitored for damage and recorded during the entire test via the Dino-lite microscope camera (M7915MZTL). The test ends when significant damage is spotted, followed by reviewing the video to measure the time to failure state, as detailed in [29]. The number of impacts, N, is calculated using Eq. (4), where t is the testing duration until failure, and R_i is the impact rate.

$$N = t \cdot R_i \tag{4}$$

The impact velocity was set to 160 m s^{-1} and the impact rate to 1 Hz.

The mass loss measurements were performed as described in [13]. An analytical balance (XS204, Mettler-Toledo Ltd., USA) with a precision of ±0.1 mg was used for the mass measurements. The initial sample weight was measured directly before the SPIFT. For each measurement the impact count was noted, the sample was unmounted from the holder, weighed on the balance and mounted again. The impact number intervals between the weight measurements started with 100 to 250 impacts at the beginning of the SPIFT and increased to 350 to 800 impacts at higher total impact counts.

During the SPIFT, a piezoelectric acoustic emission sensor, mounted to the sample holder front face as shown in Fig. 2 (a) and a PAC 18-bit A/D, 1 kHz–3MHz PCI-2 DAQ were used to measure the acoustic emission of impacts, that is transferred via the sample and sample holder to the sensor. Acoustic emission refers to the elastic stress waves that travels through the material upon impact or other processes releasing mechanical energy into the system, like material cracking [28]. Due to the sensor's position, the sensor was measuring surface waves induced by the impacts. More details on the measuring setup can be found in [28].

The measured area under the rectified signal envelope (MARSE) was used for determining the energy of the measured acoustic emission and is referred to as acoustic energy.

2.6. Microscopy

After the SPIFT, optical microscope images were taken of the samples' cross sections. The samples were cut a few millimeters away from the center of the impact damage and ground to the center with gradually finer sandpaper, finishing with a 10 µm diamond polish. The cross section images were made by image stitching of several individual micrographs taken with a DeltaPix microscope.

3. Results

3.1. Fiber volume fraction and areal porosity

Table 2 summarizes the properties of the samples tested. It distinguishes between top and base layer, showing the layer thickness

Table 2
Composite properties and quantification of voids/areal porosity in Fig. 3; The thickness uncertainty of the layers is estimated to be ±0.15 mm; Voids are approximated as spheres with circular cross sections (s. Eq. (3)).

		GF	H-FF	H-FF$_{ND}$	H-AF
Top layer	Thickness [mm]	1.20	1.25	1.55	1.45
	Fiber vol. fraction [%]	46 ± 6	27 ± 3	22 ± 2	46 ± 5
GF base layer	Thickness [mm]	4.10	4.25	4.15	4.25
	Fiber vol. fraction [%]	52 ± 2	50 ± 1	52 ± 1	50 ± 2
Porosity	Number of voids	1	33	46	48
	Average diameter [μm]	215	115 ± 50	130 ± 40	100 ± 35
	Areal porosity [%]	0.071 ± 0.001	0.81 ± 0.01	1.24 ± 0.02	0.82 ± 0.01

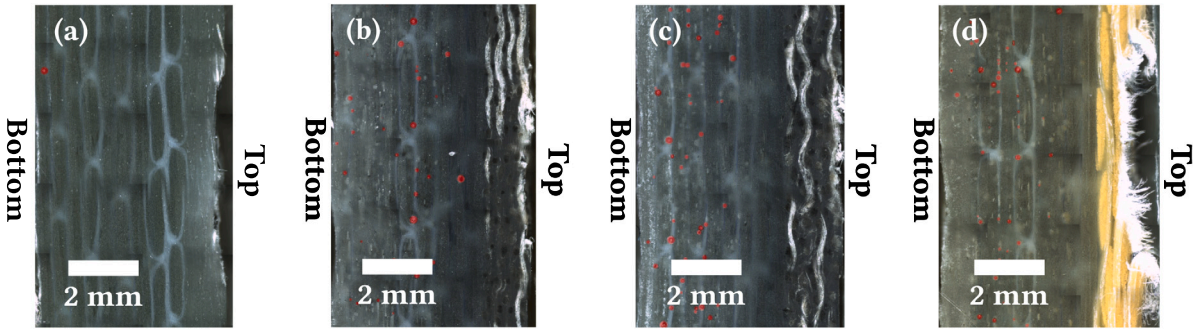

Fig. 3. Cross sections of GF (a), H-FF (b), H-FF$_{ND}$ (c) and H-AF (d) samples after about 2000 impacts; The impact velocity was 160 m s^{-1}; The image sections show the full thickness of the samples in the damage region; Voids are emphasized in red; No voids are visible at the impacted top layers; H-AF sample (d) shows severe material loss of matrix and reinforcement, while the flax samples have the least visible damage.

and the fiber volume fraction, according to Eq. (2). The base layer thickness has an average of (4.2 ± 0.1) mm, indicating the common variations within composites due to reinforcement fabric inhomogeneities and the vacuum infusion fabrication. Including the uncertainty of the measurement, the thickness uncertainty of the layers is estimated to be ±0.15 mm. It can be seen that the thickness and fiber volume fraction of the base layer of all samples are the same (overlay within error bars), which was intended with the layup during fabrication, see Section 2.3.

Fig. 3 shows cross sections of the three hybrid composite samples and the reference GF sample. The samples are shown in the region of the impact fatigue damage, depicting the full sample thickness. The damage is described in more detail in Section 3.3. The macroscopic voids that are visible in the cross section images are emphasized in red, their number and average size as well as the areal porosity are listed in Table 2. It is apparent for all samples that voids are just located in the base layer. Furthermore, there is no significant difference in void size of the hybrid samples compared to each other, but their areal porosity is higher compared to the reference GF sample.

3.2. Impact fatigue

Fig. 4 shows images of the samples' front faces during the SPIFT. They are extracted stills from the recorded tests and are given with the number of impacts at the point at which the samples experience three defined damage stages: (i) first visual damage, (ii) first matrix material loss and (iii) ring fracture.

GF and H-AF show the typical bright reflections indicating delamination and dark stains from the projectile debris after the first matrix material loss. The flax samples show bright impact imprints at the fiber locations, dark spots (accumulated debris) and bright reflections (chipped off matrix material) at the formation of cracks and matrix material loss. All samples eventually show ring fracture/island formation typical for single point impact as reported in [13,30]. The H-AF sample has a similar performance to the GF sample, but reaches the first two damage stages after about 25% less impacts. On average, H-FF$_{ND}$ withstand 9 ± 3 times as many impacts as H-AF, 6.7 ± 1.1 times as many impacts as GF and 2.2 ± 0.9 times as many impacts as FF to reach the same damage stage.

The first matrix material loss is a visual indicator for the end of the damage incubation period. According to Fig. 4 the incubation period for the GF sample is 23 impacts, for the H-FF sample it is 107 impacts, for the H-FF$_{ND}$ sample it is 181 impacts and for the H-AF sample it is 16 impacts.

3.3. Mass loss

The mass loss of the hybrid composites as well as the reference bulk GF composite is shown in Fig. 5, plotted against the number of impacts. The mass loss of the bulk FF and FF$_{ND}$ material, reported in [13], is also shown for comparison. The mass loss measurements give important information about the progression of erosion and easily show differences between the materials in erosive damage and proneness to material failure.

The data shows that the H-AF and the GF sample have significantly higher, and stronger increasing mass loss compared to the hybrid flax samples. Fig. 5 (b) indicates that H-AF has a shorter incubation period than GF, which was shown in Fig. 4. Furthermore, Fig. 5 (b) shows that untreated and nanodiamond-treated flax samples start losing mass at less than 100 impacts and more than 200 impacts, respectively. Although not matching exactly the damage incubation shown in Fig. 4, the same tendency is depicted. Thus, the H-AF and GF composites are more prone to material failure than the hybrid flax composites.

The mass loss data in Fig. 5 is well fitted with a power function, $f(x) = a(x - x_0)^c$ (see Table 3 for respective fitting parameters), which is shown with confidence intervals of one standard deviation (shaded). However, because of missing data, the incubation period cannot be modeled reasonably, which applies particularly to the H-AF data. The large and unusual shaped confidence intervals at the end of the incubation period (beginning of mass loss) are a result of the uncertainty of the parameter x_0 and possible negative values in the root/power function ($c < 1$).

At an interpolated impact count of 1950, H-AF, H-FF and H-FF$_{ND}$ have (113.2 ± 0.4)%, (14.5 ± 0.2)% and (7.3 ± 0.4)% of the mass loss of GF, respectively. This ratio is relatively constant between 1000 and 1950 impacts.

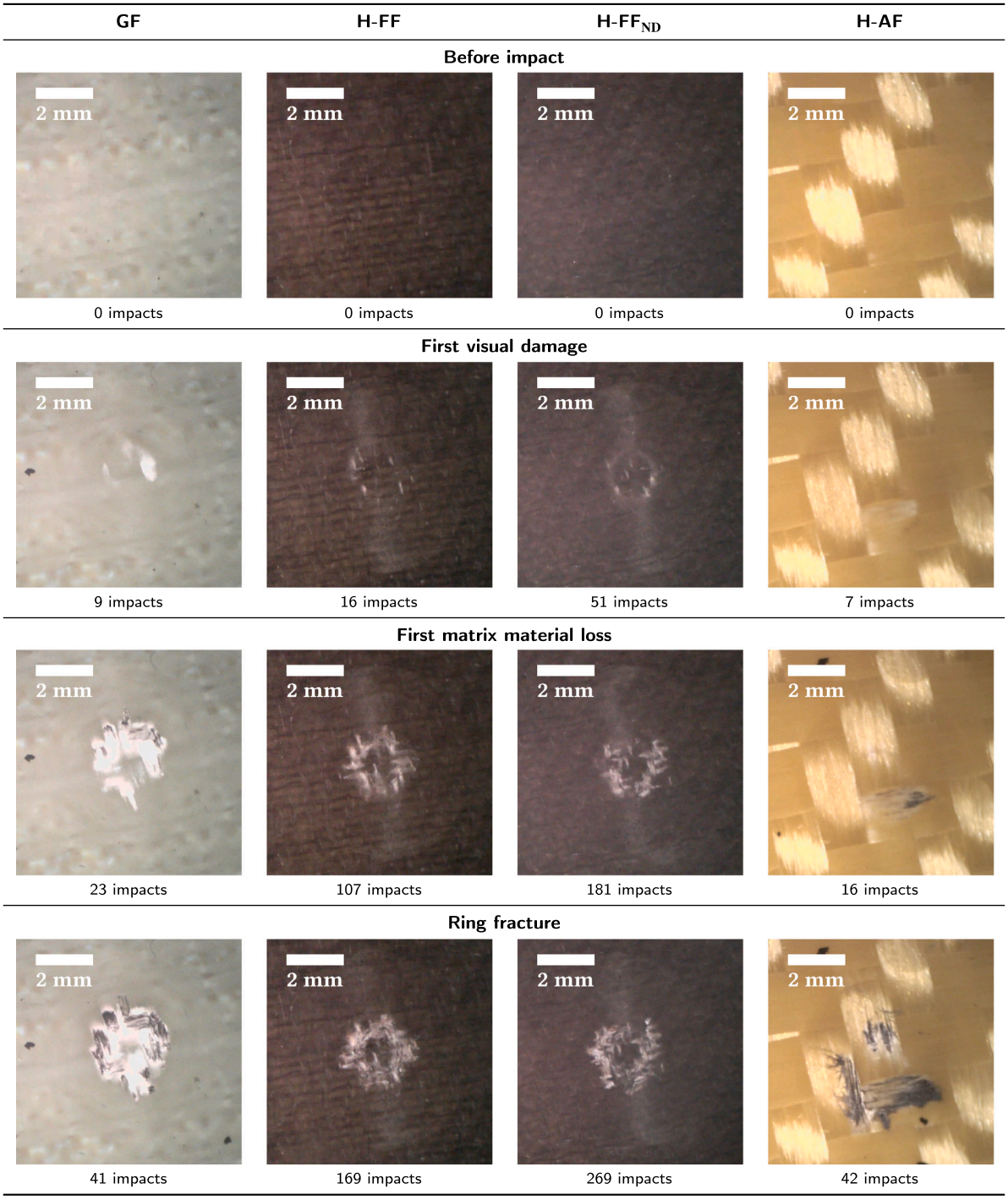

Fig. 4. Visual extent of three early damage stages of impact testing ($v = 160\,\mathrm{m\,s^{-1}}$); Images are extracted stills during testing, from the DinoLite microscope; H-FF$_{ND}$ withstands the most impacts to reach the same damage stage, while H-AF is in the same range as GF.

Table 3
Fitting parameters of function $f(x) = a(x - x_0)^c$, fitted to mass loss data in Fig. 5.

	H-AF	GF	H-FF	FF	H-FF$_{ND}$	FF$_{ND}$
a [mg]	$(7 \pm 2) \cdot 10^{-2}$	$(11 \pm 2) \cdot 10^{-2}$	$(15 \pm 6) \cdot 10^{-2}$	$(1.1 \pm 0.4) \cdot 10^{-2}$	$(2.0 \pm 3.5) \cdot 10^{-2}$	$(2.5 \pm 0.1) \cdot 10^{-2}$
x_0	-1 ± 9	99 ± 4	150 ± 60	0 ± 7	350 ± 200	640 ± 45
c	0.71 ± 0.04	0.63 ± 0.02	0.33 ± 0.06	0.71 ± 0.05	0.5 ± 0.2	0.46 ± 0.07

The strong difference between GF and H-AF is also clearly visible in Fig. 3, where the cross sections of the samples are shown after about 2000 impacts. GF (Fig. 3 (a)) and H-AF (Fig. 3 (d)) have pronounced impact craters. The damage and fiber loss are more severe for H-AF, where the top layer is eroded to almost halve of its initial thickness. This is in strong contrast to the H-FF (Fig. 3 (b)) and H-FF$_{ND}$ (Fig. 3 (c)) samples, that just show a few matrix cracks and onset of weak fiber damage.

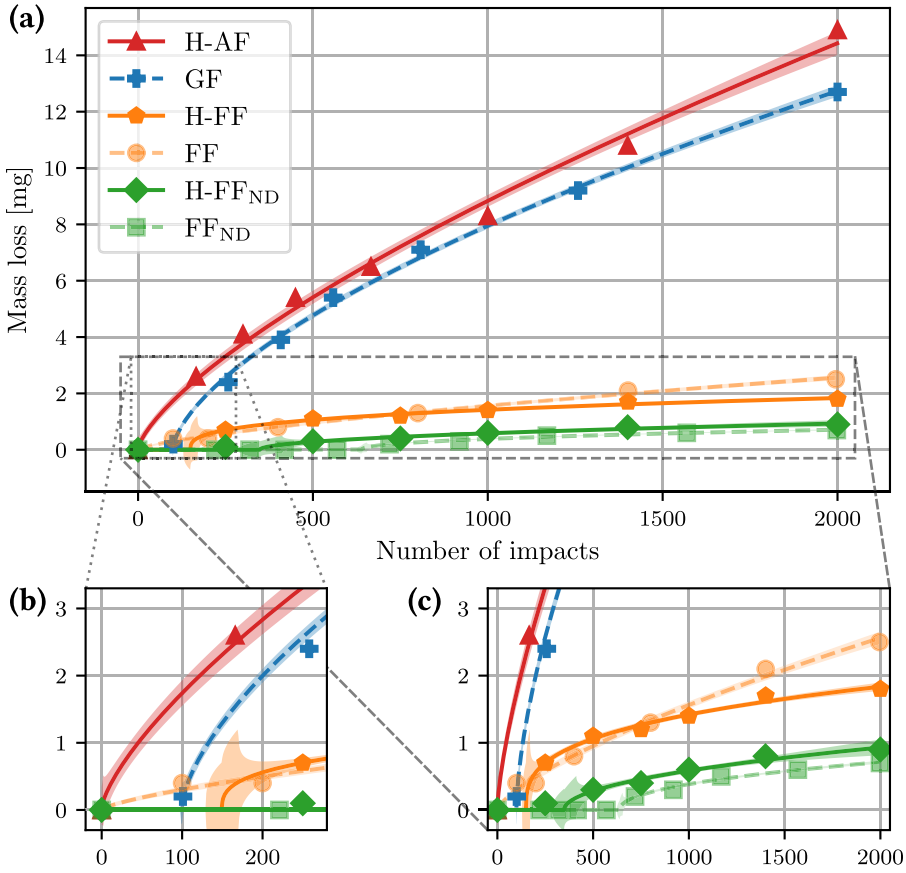

Fig. 5. (a) Mass loss as a function of impact number with $v_{impact} = 160\,m\,s^{-1}$; Mass errors are too small to be shown ($\Delta m = \pm 0.1$ mg); A power function, $f(x) = a(x - x_0)^c$, is fitted to the data, shown with one standard deviation confidence intervals (shaded); (b) Damage incubation period (c) Comparison between flax hybrid composites (H-FF, H-FF$_{ND}$) and bulk material composites (FF, FF$_{ND}$) from [13].

Table 4
Average values of frequency, peak amplitude, duration and energy of recorded acoustic emissions for the damage incubation (*inc*) according to Fig. 4 and for the interval between incubation and 2000 impacts (*rest*); The most distinct difference between the materials is shown during the damage incubation and for their acoustic energy.

	GF	H-FF	H-FF$_{ND}$	H-AF
Frequency$_{inc}$ [kHz]	77 ± 1	77 ± 1	78 ± 1	76 ± 1
Frequency$_{rest}$ [kHz]	76 ± 1	76 ± 2	76 ± 1	75 ± 2
Amplitude$_{inc}$ [dB]	93 ± 1	95 ± 1	95 ± 1	92 ± 1
Amplitude$_{rest}$ [dB]	95 ± 1	95 ± 2	95 ± 1	95 ± 2
Duration$_{inc}$ [ms]	43.9 ± 0.9	43.6 ± 0.5	43.4 ± 0.6	43.4 ± 0.4
Duration$_{rest}$ [ms]	43.5 ± 0.7	43.4 ± 1.2	43.4 ± 0.6	43.2 ± 1.1
Energy$_{inc}$ [A.u.]	444 ± 25	490 ± 20	545 ± 20	365 ± 10
Energy$_{rest}$ [A.u.]	505 ± 25	490 ± 20	580 ± 15	460 ± 40

3.4. Acoustic energy

Table 4 shows the average values of frequency, peak amplitude, duration and energy of the recorded acoustic emissions for the damage incubation and for the interval between incubation and 2000 impacts. It can be seen that the most distinct difference between the materials is shown for their acoustic energy. This can be explained by the fact that the acoustic energy combines frequency, duration, amplitude and signal shape in one value.

In Fig. 6 (a) the average acoustic energy is depicted during the damage incubation according to Fig. 4 and during the consecutive intervals of 0–100, 100–200 and 200–2000 impacts. It shows that the difference between the materials is strongest during the damage incubation, which can be explained by the absence of damage. Since the damage progression, e.g. mass loss and creation of impact craters (Fig. 3), is different for the tested materials, the least geometric difference and damaged caused interference is given in the beginning of the SPIFT. This is in line with previous acoustic emission recordings during the SPIFT [28].

In the incubation period and the first 100 impacts H-FF$_{ND}$ has the highest acoustic energy, followed by H-FF, GF and H-AF.

Since high-velocity impact response is dominated by stress wave propagation through the material [31], the impacts during the SPIFT are most likely the strongest source for the measured acoustic emissions. However, failure modes (matrix cracking, delamination, fiber breakage) and material damage in general, are also sources for acoustic emission [32–34]. Therefore, the measured increase in acoustic energy with the impact number can indicate changes and potential damage in the samples. The GF sample, for instance, shows an increase in acoustic energy in the 100–200 impact interval, Fig. 6 (a), that coincides with the onset of stronger mass loss, Fig. 5 (b). In the further course of the SPIFT, the acoustic energy of GF, H-FF and H-AF approach each other and reach the same acoustic energy (overlay within error bars) in the damage interval of 200–2000 impacts. Only the H-FF$_{ND}$ sample has a clear offset in acoustic energy throughout the SPIFT.

Each failure mode has a different acoustic emission spectrum, being dependent on the materials tested [32–34]. However, this could not be detected in the SPIFT, which can be explained by the different measuring setup and test mode used in this test. For the identification of failure modes, the sensors are usually mounted on the samples and standard coupon tests like tensile or bending tests are performed [32–34], that do not create stress waves in contrast to high-velocity impacts.

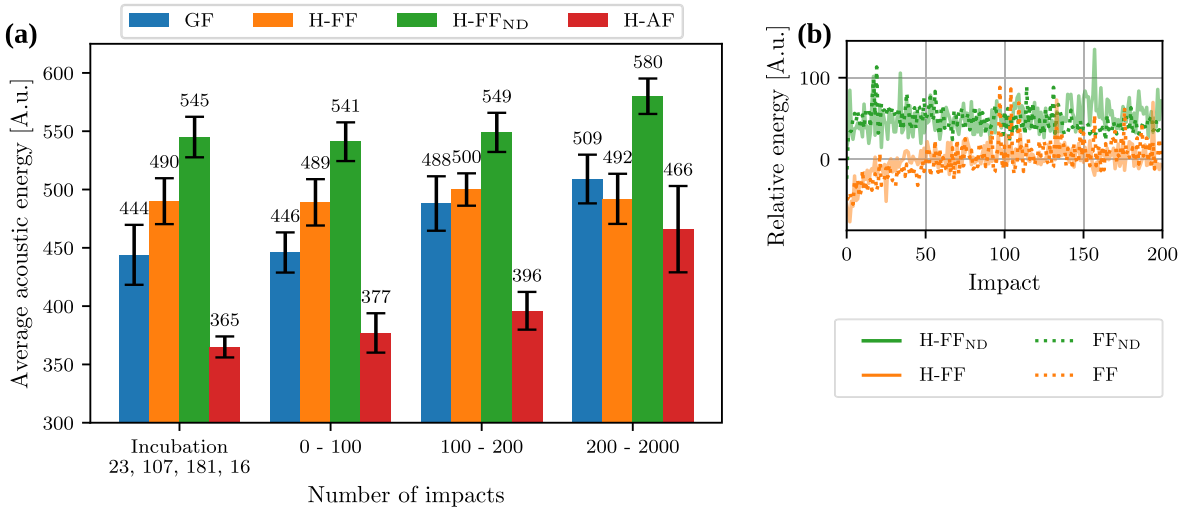

Fig. 6. (a) Average acoustic energy during the damage incubation according to Fig. 4 and during the consecutive intervals of 0–100, 100–200 and 200–2000 impacts, showing most distinct differences before severe damage; AF absorbs the most impact energy ($v_{impact} = 160\,m\,s^{-1}$), resulting in the strongest damage; Nanodiamonds help to dissipate the impact energy and reduce damage; (b) Comparison of impact energy between hybrid sample (H-FF, H-FF$_{ND}$) and bulk sample (FF, FF$_{ND}$) relative to average values of the untreated flax samples (H-FF, FF) in the depicted interval; The acoustic energy progression for hybrid and bulk samples is almost identical.

Even though invisible damage can add to the acoustic emission during the damage incubation, it can be assumed that the acoustic emission is dominated by stress waves that were caused by the impacts. The initial impact pressure is dependent on the composite density and was calculated to be 14% lower for bulk FF composites compared to bulk GF composites, because of the lower density of FFs compared to GFs [13]. Since AFs have a density close to FFs (see Table 5), it can be assumed that the impacts create a similar level of acoustic emission (±10%) for all samples. Thus, different acoustic energies result mostly from the transmission/absorption properties of the different materials. As consequence, low acoustic energy corresponds to less transmission and more absorption of the impact energy by the tested material. It is apparent that materials with high impact fatigue and mass loss have less acoustic energy. This indicates a relation between impact energy absorption and material failure.

For comparison, the acoustic energy of the bulk materials FF and FF$_{ND}$ was also measured and included in Fig. 6. Due to a shift in absolute energy, which we ascribe to a different structural damping between sample and sample holder (different sample size, mounting position and/or contact pressure), the acoustic energy is given relative to the interval's average acoustic energy of the untreated flax samples FF and H-FF. This is shown in Fig. 6 (b). The difference in acoustic energy between FF and FF$_{ND}$ is almost identical to the difference between H-FF and H-FF$_{ND}$.

Differences in acoustic energy can be caused by a number of material properties, affecting the transmission of elastic waves, their damping and absorption. The matrix and fiber materials as well as their interface play an important role, since the components pass on their properties to the composite. In the following the velocity of elastic waves, their reflectivity at the interfaces between matrix and fiber, and energy absorption due to material failure are analyzed.

3.4.1. Elastic wave velocity

Impact creates longitudinal compression waves (c), transversal shear waves (c_S), and Rayleigh surface waves (c_R) propagating through the material with different velocities [44]. The wave velocity gives information about the energy dissipation and the acoustic energy, since the wave energy is proportional to the wave velocity [45]. In turn, the wave velocities are dependent on the elastic properties and the density of the materials, which are listed in Table 5 for cured epoxy resin, GF, FF, AF and diamond (D).

The compression wave velocity (speed of sound) in a solid is given by

$$c = \sqrt{\frac{E(1-\nu)}{\rho(1+\nu)(1-2\nu)}}, \tag{5}$$

with E being the elastic modulus, ρ being the density and ν being the Poisson's ratio [46].

Due to the position and alignment of the piezoelectric sensor, mostly surface waves were measured during the SPIFT. Therefore, the Rayleigh wave velocity is of particular interest. It can be approximated by

$$c_R = \frac{0.862 + 1.14\nu}{1+\nu} c_S \quad \text{with } c_S = \sqrt{\frac{G}{\rho}}, \tag{6}$$

with G being the shear modulus [47].

The calculated wave velocities are listed in Table 6. The high wave velocities of diamond can explain the higher acoustic energy measured for the H-FF$_{ND}$ and FF$_{ND}$ samples compared to the untreated flax samples (see Fig. 6 (b)). The slightly higher average frequency (f) of H-FF$_{ND}$ (Table 4), indicates a higher wave velocity through the nanodiamond treatment, since $c = f \cdot \lambda$, with λ being the wavelength. Furthermore, the higher wave velocities of GF match the higher acoustic energy compared to AF/H-AF.[1] However, H-FF has a higher acoustic energy than GF and H-AF, despite having lower wave velocities.[1]

3.4.2. Wave reflectivity

In a previous work [13], the reflection coefficients of GF and FF were calculated as -0.71 ± 0.02 and -0.21 ± 0.08, respectively [13], predicting less transmission for compression waves in GF composites.

In order to find a correlation between wave reflectivity and acoustic energy (mostly surface wave energy, due to sensor position), this needs to be applied to shear and Rayleigh waves, too. The reflection coefficient at the interface of matrix (M) and fiber (F) is defined as

$$R = \frac{Z_M - Z_F}{Z_M + Z_F}, \tag{7}$$

with $Z = \rho c$ being the acoustic impedance [45].

The reflection coefficients for the different elastic waves are listed in Table 7. It shows that shear and Rayleigh waves have about the

[1] Here, we refer to the transversal (TV) direction of AF/FF, since the compression waves hit the fibers mainly in this direction due to the composite layup.

Table 5
Material properties of the single materials; FF and AF are an-isotropic, relevant properties are given as longitudinal (LT) with and transversal (TV) to the fiber direction.

	Epoxy resin	GF	FF	AF	D
E_{LT} [GPa] E_{TV} [GPa]	2.9 ± 0.3 [35]	70 ± 6 [36]	54 ± 15 [36] 7 ± 2 [36]	112.4 [27] 8 [38]	1130 ± 80 [37]
G_{LT} [GPa]	1.0 ± 0.1[a]	35.42 [38]	2.5 [39]	3 [38]	502 [37]
ρ [g cm^{-3}]	1.1 ± 0.2 [35]	2.617 ± 0.005 [25]	1.59 ± 0.05 [26]	1.44 [27]	3520 [37]
ν_{LT} ν_{TV}	0.4 [40]	0.21 ± 0.01 [40,41]	0.3 [42] 0.32 [43]	0.36 [27] 0.37 [38]	0.07 [37]

[a] Calculated by $G = \frac{E}{2(1+\nu)}$.

Table 6
Calculated velocities [m s^{-1}] of compression wave (c) longitudinal (LT) with and transversal (TV) to the fiber direction, Eq. (5), shear wave (c_S) and Rayleigh wave (c_R), Eq. (6).

	Epoxy resin	GF	FF	AF	D
c_{LT} c_{TV}	2400 ± 150	5800 ± 300	6800 ± 950 2500 ± 400	11 450 3050	$18\,000 \pm 640$
c_S	970 ± 50	3679 ± 4	1250 ± 20	1440	11 940
c_R	910 ± 50	3349 ± 8	1160 ± 20	1350	10 510

Table 7
Calculated reflection coefficient of compression wave (R) longitudinal (LT) with and transversal (TV) to the fiber direction, shear wave (R_S) and Rayleigh wave (R_R), Eq. (7).

	GF	FF	AF	D
R_{LT} R_{TV}	-0.71 ± 0.02	-0.61 ± 0.05 -0.21 ± 0.08	-0.73 ± 0.02 -0.27 ± 0.03	-0.92 ± 0.01
R_S	-0.80 ± 0.01	-0.30 ± 0.03	-0.32 ± 0.02	-0.951 ± 0.003
R_R	-0.79 ± 0.01	-0.30 ± 0.03	-0.32 ± 0.02	-0.947 ± 0.003

same reflection coefficient at the matrix–fiber interface, which is higher than for compression waves.[1] Thus, GFs reflect shear and Rayleigh waves about 3 times as strong as FFs. Stronger reflections mean that less wave energy arrives at the sensor, which can explain the lower measured acoustic energy of the GF sample compared to the H-FF sample, shown in Fig. 6 (a). As consequence, the impact energy dissipates less and higher peak stress in the impact area might explain why the matrix/surface is damaged faster in GF composites compared to FF composites [13]. Thus, the acoustic energy measurements support the hypothesis, that a high reflectivity and thus low transmission of stress waves within the composites causes faster damage [13].

However, this argument cannot be applied to the H-AF and H-FF_{ND} samples, because they show the lowest and highest acoustic energy, respectively. AFs have an-isotropic properties [9] similar to FFs [39] (see Table 5), resulting in a lower speed of sound in transversal (TV) direction and a lower compression reflection coefficient compared to the longitudinal (LT) direction. All three reflection coefficients of AFs are as low as of FFs, but the acoustic energy of H-AF was even lower than of GF, indicating less wave transmission. On the contrary, the high reflection coefficients of diamond predict low stress wave and acoustic energy transmission, which is not matching the acoustic energy measurements.

This indicates that there are other causes that are more decisive for the acoustic energy transmission of the H-AF and H-FF_{ND} samples than the stress wave reflectivity. We discuss this in more detail in the following.

3.4.3. Energy absorption due to material failure

Material failure during the SPIFT can be a reason for different acoustic energy measurements. Delamination (see Fig. 4) and breakage of fibers (see Fig. 3) were observed during the SPIFT and are both known for their energy absorption and impact damping abilities [48].

Delamination can occur due to poor interfacial adhesion between matrix and fiber [11], which is a known property of AFs [49]. Furthermore, material failure is a main mechanism for impact energy absorption of composites [50]. This is utilized and studied for protective anti-ballistic applications of AF composites [51–53]. A consequence of the energy absorption due to material failure is the high mass loss of the H-AF sample, which is shown in Fig. 5. This can explain why the H-AF sample had the lowest measured acoustic energy and showed the highest impact fatigue and mass loss during the SPIFT.

Material failure as a major contribution to impact energy absorption, can qualitatively explain the acoustic energy of the GF, H-FF and H-FF_{ND} samples, too. The GF sample has a similar mass loss as the H-AF sample (see Fig. 5), but a higher acoustic energy (see Fig. 6). This correlates with less fiber failure and less broken fibers, which is shown in Fig. 3, where the impact crater of the H-AF sample is almost twice as deep compared to the GF sample. Furthermore, because of the higher density of glass compared to AFs, the amount of broken fibers of the GF sample must be lower compared to the H-AF sample at a similar mass loss.

Both flax samples have only little mass loss and no visible fiber failure as shown in Fig. 3. Hence, less energy absorption due to less material failure can explain the higher acoustic energy compared to the GF sample.

The treatment of flax with nanodiamonds was shown to have a positive effect on the tensile strength of FF_{ND} compared to untreated flax [16] and was shown to improve the impact resistance of FF_{ND} composites [13]. This results in less fiber failure [13], which is also reflected in the higher acoustic energy of the H-FF_{ND} and FF_{ND} samples compared to H-FF and FF samples, Fig. 6 (b).

4. Discussion

4.1. Comparison of hybrid and bulk material composites

It is very interesting to see that the SPIFT results of the hybrid and bulk material composites [13] are almost identical. For instance, the first visual matrix material loss of FF and FF_{ND} composites occurred after 106 and 179 impacts at a velocity of 160 m s^{-1}, respectively [13]. The hybrid H-FF and H-FF_{ND} composites, studied in this work, reached the same damage under the same conditions after 107 and 181 impacts, respectively. This is visualized in Fig. 7, where the V-N data of hybrid composites and V-N fits of bulk composites [13] are shown. On average the incubation period at 160 m s^{-1} is 4.63 ± 0.02 times (FF, H-FF) and 7.83 ± 0.04 times (FF_{ND}, H-FF_{ND}) the incubation period of the reference GF composite.

In Fig. 5 (c) the mass loss of hybrid H-FF and H-FF_{ND} composites is compared to the bulk material FF and FF_{ND} composites. Both hybrid samples are very close to their respective bulk sample values. Especially the nanodiamond-treated samples (H-FF_{ND}, FF_{ND}) have an almost constant difference of (0.20 ± 0.15) mg, which just is slightly more than the mass measurement error of 0.1 mg can resolve. The H-FF sample, on the other hand, starts to deviate after an impact count of about 1000 and has less mass loss than the bulk sample with maximum difference of about (-0.70 ± 0.15) mg.

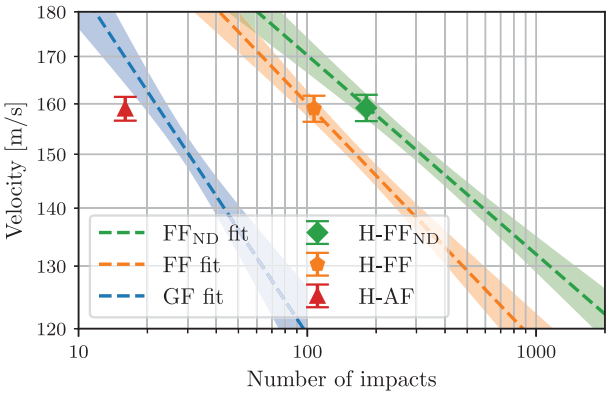

Fig. 7. V-N data of hybrid composites and V-N fits of bulk composites with 95% confidence intervals (shaded) [13]; While the H-AF data is outside of the GF fit, indicating worse fatigue properties, H-FF and H-FF$_{ND}$ match the fit of the respective bulk materials.

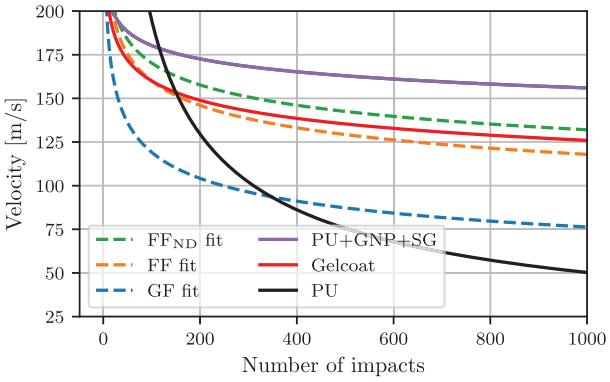

Fig. 8. Comparison of V-N fits, Eq. (8), of bulk GF, FF and FF$_{ND}$ composites [13] with V-N fits of an erosion protective gelcoat [28] and two PU coatings [29]; All V-N data describes the point of first material loss; The non-logarithmic depiction shows more intuitively the difference in erosion resistance of the different materials, with PU performing best in the high velocity range (>175 m s^{-1}) and PU+GNP+SG performing best at lower velocities. FF$_{ND}$ performs better than the gelcoat at all velocities and has a much higher resistance than PU at the velocities relevant for wind power (<150 m s^{-1}).

In summary, it can be stated that a thin flax composite layer of about 1.5 mm gives hybrid composites the same superior fatigue resistance as the bulk flax material and that the V-N curves of hybrid H-FF$_{ND}$ composites are very likely similar to the bulk material V-N curves [13], which is indicated in Fig. 7.

This can be explained by the impact energy mostly dissipating at the surface of the composites. This is supported by [54] who showed in a general context that ~2/3 of the power of elastic waves generated in a material are contained in Rayleigh surface waves. Another indication are the acoustic energy measurements, Fig. 6 (b), with almost no difference between hybrid and bulk samples, showing that the nanodiamond treatment causes higher acoustic energies independent of the flax thickness.

4.2. Comparison to protective coatings

Fraisse et al. [28] and Frost-Jensen Johansen et al. [29] used the SPIFT to test composite coatings on their erosion protective properties. This allows a direct comparison between these coatings and the hybrid/bulk composites presented in this work and [16]. Fig. 8 shows a comparison between fits of the V-N data of bulk GF, FF and FF$_{ND}$ composites [13] and V-N fits of a composite gelcoat [28] and two composite PU coatings, pure PU and, graphene and sol gel-modified PU (PU+GNP+SG) [29]. More information about the coatings can be found in the respective references. All fits are based on the same equation

$$N(v_{\text{impact}}) = C \cdot v_{\text{impact}}^{-m} \tag{8}$$

where N is the number of impacts, v is the impact velocity and, C and m are the fitting parameters. All data describes the point of first material loss.

It can be seen that the PU coating performs best in the high velocity range (>175 m s^{-1}), while the PU+GNP+SG coating shows the highest damage resistance at lower velocities, which is more relevant for the use on wind turbine blades. FF$_{ND}$ performs better than the gelcoat at all velocities and has a much higher resistance than PU at the lower velocities relevant for wind power (<150 m s^{-1}). FF comes close to the performance of the gelcoat.

This shows the great potential of combining H-FF and H-FF$_{ND}$ composites with a top coating for leading edge protection of wind turbine blades.

Table 8
Summary of the discussed properties, showing which property can predict the right order in the acoustic energy of the different composites (+).

	GF	H-FF	H-FF$_{ND}$	H-AF
Elastic wave velocity	+	−	+	+
Wave reflectivity	+	+	−	−
Material failure	+	+	+	+

4.3. Absorption of impact energy

The acoustic energy measurements help to understand how the impact energy of the rubber ball projectile is absorbed in the different composite materials. In Table 8 the regarded properties are summarized and it is shown which property is able to predict the right order in the acoustic energy of the different composites, Fig. 6.

The different elastic wave velocities of the stress wave that is created upon impact, can explain the order of acoustic energy of all materials except for the H-FF composite. However, it cannot explain the rise in acoustic energy with the progressing impact number.

The high reflection coefficient of GFs can explain why the GF composite has less transmission of elastic waves and less measured acoustic energy compared to FFs. But wave reflectivity on its own cannot bring the H-AF and H-FF$_{ND}$ composites in line with the acoustic energy measurements. However, the discussed properties are connected to each other. While the wave reflectivity is dependent on the wave velocity, Eq. (7), a higher reflectivity can lead to higher peak stress and earlier material failure.

Material failure in turn can be the link in the correlation between high mass loss and low acoustic energy transmission/high impact energy absorption. An explanation for this can be found in the different fiber structures of GFs, FFs and AFs as well as in the effect of nanodiamonds on FFs, which will be discussed now.

4.3.1. Fiber structure

In contrast to GFs, FFs [55] and AFs [38] are both an-isotropic and significantly weaker in the transverse fiber direction. AFs are made from polymer chains that have no covalent bonds between the polymer chains, just weak intermolecular hydrogen bonding [56]. FFs have a multi-scale and hierarchic structure, where cellulose microfibrils in a matrix of hemicellulose and lignin form cell walls that enclose the lumen, a hollow channel in the fiber center [57]. Flax shows non-destructive impact energy absorption, due to its hierarchic structure and viscoelastic nature. The impact energy can dissipate through friction and is transformed into heat on different scales: (i) fabric, (ii) yarn, (iii) fiber, (iv) cell wall, (v) lumen and (vi) micro fibril. This is described in detail in [13] and gives flax composites better vibration

Table 9
Bulk modulus, B, calculated with Eq. (9) and compressive strength, σ_c, of the single materials; Where applicable properties are given as longitudinal (LT) with and transversal (TV) to the fiber direction.

	Epoxy resin	GF	FF	AF
B_{LT} [GPa]	4.8 ± 0.5	45 ± 5	45 ± 13	134
B_{TV} [GPa]			7 ± 2	10
σ_c [MPa]	102 [38]	1550 [38]	1200[a] [57]	600[a] [57]

[a] Measured with loop test.

damping [58] and sound absorption [59] properties compared to GF composites.

Looking at the compression properties of the different fibers can help quantifying the difference in structure. The bulk modulus, B, describes the effort of reducing the volume of a material and can be estimated from the elastic modulus, E, and the Poisson's ratio, ν, [46]:

$$B = \frac{E}{3(1-2\nu)} \tag{9}$$

The calculated values are listed in Table 9, together with compressive strength values that were found in literature. It is apparent that GFs have a higher bulk modulus and compressive strength than FFs and AFs in the transversal fiber direction. This can explain why GFs have a higher fiber failure resistance than AFs. The fact that GFs fail faster than FFs however, can be understood together with GF's high stress wave reflectivity that causes stress peaks, overcoming the fiber's strength.

The lumen in FFs strongly affects compressability, since it provides volume for compression, explaining the low bulk modulus. The lumen might also act as a built-in air cushion, giving the fiber the ability to recover between impacts.

Even though the AF bulk modulus is slightly higher than of flax, its compressive strength is just halve as high as of flax. Therefore, the faster fiber damage and failure under impact is likely a result of the low compressive strength [9,57]. Furthermore, it is reported that AFs do not recover well from strain and experience fiber splitting, fraying and fast damage [9]. This behavior can also be seen in the cross section image of the damaged H-AF sample in Fig. 3 (d) and is a channel for destructive energy absorption.

4.3.2. Nanodiamonds

It was shown in [16] that through the nanodiamond treatment of flax, nanodiamonds bond to flax, improving the cohesion between the fibers in the yarn and fabric. This increases the friction between the fibers and strengthens the yarn. The increase in friction through nanodiamonds is likely enhancing the non-destructive energy dissipation in several of the mentioned structure levels of flax and results in less material failure, as shown in [13]. The higher acoustic energy of the H-FF_{ND} sample compared to the H-FF sample supports this hypothesis.

The higher acoustic energy also indicates that nanodiamonds improve the compatibility between the matrix and the treated fibers, since the matrix–fiber-interface is important for load transmission [48] and the acoustic energy transmission increased after the nanodiamond treatment of flax.

4.4. Aramid or flax fibers for erosion protection?

The SPIFT results show that the H-AF composite performs worse than the reference GF composite, with a 30% shorter erosion incubation period and more than 13% higher mass loss at impact velocities of 160 m s^{-1}. This is also shown in Fig. 7, where the H-AF data is clearly outside of the 95% confidence intervals of the GF fit. Together, this indicates adverse erosion properties when applied to wind turbine blades. Thus, despite the promising qualities (high impact resistance and toughness, low density, electrically non-conducting), we demonstrate that AF composites are not suitable for leading edge protection.

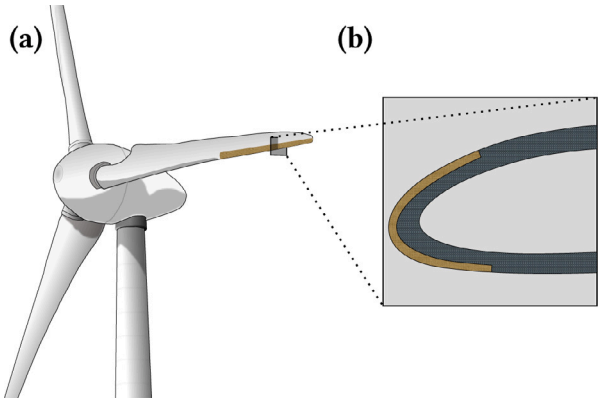

Fig. 9. (a) Sketch of wind turbine with FF_{ND} skin layer (brown) on the blade's leading edge at the outermost blade section (about 30 m length) towards the tip; (b) Turbine blade cross section (not at scale) showing the hybrid composite at the leading edge, a thin layer of FF_{ND} (brown; about 1.5 mm thick and 0.5 m wide over leading edge) on top of the base GF (blue); The rest of the blade is made conventionally from GF to keep the blade's mechanical properties unchanged. (For interpretation of the references to color in this figure legend, the reader is referred to the web version of this article.)

In strong contrast to this, the H-FF_{ND} composite has an almost 8 times as long erosion incubation period and at least 96% less mass loss at impact velocities of 160 m s^{-1} compared to GF composites.

4.5. Failsafe skin layer for wind turbine blades

Leading edge erosion (LEE) gains severity with longer wind turbine blades and higher tip speeds. The 15 MW offshore reference wind turbine defined by the International Energy Agency (IEA) [19] has a rotor diameter of 240 m with a maximum tip speed of 95 m s^{-1}. Erosion occurs especially towards the tip of blade, where the velocity is higher. Here, there is need for extra protection, which might only include the last 30 m towards the tip, covering speeds from 95 m s^{-1} to about 70 m s^{-1}. This is sketched in Fig. 9 (a), where a wind turbine is shown with a FF_{ND} skin layer on the leading edge towards the blade's tip.

A (1.55 ± 0.15) mm thin skin layer of FF_{ND} composite on the leading edge (e.g. 30 m length, 0.5 m width) can be easily included in the layup during the blade fabrication with just four plies of (136 ± 2) g m^{-2} FF_{ND}. In Fig. 9 (b) the blade's cross section is sketched, showing the hybrid composite at the leading edge, a thin layer of FF_{ND} on top of the base GF, while the rest of the blade is made conventionally from GF. In this way, the effect of the flax skin layer on the mechanical properties of established and well tested wind turbine blades made from GF is kept minimal. With its low density (ρ = 1160 kg m^{-3} [13]), the FF_{ND} composite layer would only add an extra weight of about 26 kg, which is less then 0.04% of the turbine blades total weight [19].

Since, the SPIFT results are almost identical, it can be concluded that hybrid composites have the same superior fatigue resistance as the bulk flax material. This means that the additional FF_{ND} skin layer potentially increases the erosion incubation period by a factor of 60 ± 20 at the maximum rotation speed of 95 m s^{-1} (extrapolated from V-N fatigue data) [13] and substantially enhances the base erosion resistance of wind turbine blades.

5. Conclusions

In this work we present the impact fatigue and mass loss of hybrid composites, build from two different fiber reinforcements. The hybrid composites consist of a thin (1.2 to 1.55 mm) top layer made from FF, FF_{ND} and AF and a thick ((4.20 ± 0.15) mm) base layer made from GF. This is compared to bulk material composites made from GF, FF and

FF_{ND}. We show that H-FF and H-FF_{ND} composites have as little impact fatigue and mass loss as FF and FF_{ND} composites reported in [13].

Compared to GF composites, H-FF_{ND} composites have an almost 8 times as long erosion incubation period and more than 96% less mass loss at impact velocities of $160\,m\,s^{-1}$. The nanodiamond treatment of flax almost doubled the incubation period of H-FF composites and halved the mass loss. In contrast to that, the H-AF composite perform worse than the GF composite, with a 30% shorter erosion incubation period and more than 13% higher mass loss. The acoustic energy transmission measured for the hybrid composites indicates that impact energy absorption due to material failure is the main reasons for the measured impact fatigue behavior. Here, the different fiber structures make the difference between destructive (GF, AF) and non-destructive (FF) energy absorption, while nanodiamonds enhance the energy dissipation.

Consequently, it can be concluded that AFs are not suitable for erosion protection of wind turbine blades. FF_{ND} on the other hand, shows great potential to be implemented as a low-cost, lightweight skin layer on the leading edge. The simple addition of four plies of FF_{ND} during the turbine blade's fabrication, would increase the mass of a turbine blade by negligible ~0.04%, while providing an increase in base erosion resistance by a factor of 60 ± 20. Thus, flax as failsafe layer could expand the repair window, reduce costs, and enhance reliability and damage tolerance.

6. Future work

Even though all top layer fiber materials were chosen to have the same weave pattern, there are differences in the textile properties between synthetic and natural fibers. It is therefore interesting to investigate different yarn properties like twist or thickness as well as non-crimp fabrics in the future.

Microscopic images of the surface layers could further reveal details on damage mechanisms and more differences between synthetic and natural fibers.

Following the indications that the impact energy mostly dissipates at the surface of composites, the performance of even thinner flax layers and the minimal thickness of the skin layer need to be studied.

As natural next step, whirling arm rain erosion tests can give further insights on the performance of FF_{ND} as protection layer for rain droplet impacts.

CRediT authorship contribution statement

Carsten Hinzmann: Conceptualization, Formal analysis, Investigation, Writing – original draft, Visualization. **Nicolai Frost-Jensen Johansen:** Conceptualization, Investigation, Writing – review & editing. **Charlotte Bay Hasager:** Conceptualization, Writing – review & editing, Supervision. **Bodil Holst:** Conceptualization, Writing – review & editing, Supervision, Funding acquisition.

Declaration of competing interest

The authors declare that they have no known competing financial interests or personal relationships that could have appeared to influence the work reported in this paper.

Data availability

Data will be made available on request.

Acknowledgments

The authors would like to thank the reviewers for their valuable feedback.

This project was funded by Equinor ASA through the "Akademiaavtale" program at the University of Bergen. Additional support was provided by the Faculty of Mathematics and Natural Science, University of Bergen.

References

[1] Brøndsted P, Lilholt H, Lystrup A. Composite materials for wind power turbine blades. Annu Rev Mater Res 2005;35:505–38. http://dx.doi.org/10.1146/annurev.matsci.35.100303.110641, URL: https://www.annualreviews.org/doi/10.1146/annurev.matsci.35.100303.110641.

[2] Keegan MH, Nash DH, Stack MM. On erosion issues associated with the leading edge of wind turbine blades. J Phys D: Appl Phys 2013;46:383001. http://dx.doi.org/10.1088/0022-3727/46/38/383001.

[3] Sareen A, Sapre CA, Selig MS. Effects of leading edge erosion on wind turbine blade performance. Wind Energy 2014;17:1531–42. http://dx.doi.org/10.1002/we.1649, URL: https://onlinelibrary.wiley.com/doi/abs/10.1002/we.1649.

[4] Bak C, Forsting AM, Sorensen NN. The influence of leading edge roughness, rotor control and wind climate on the loss in energy production. J Phys Conf Ser 2020;1618:052050. http://dx.doi.org/10.1088/1742-6596/1618/5/052050.

[5] Mishnaevsky Jr L, Thomsen K. Costs of repair of wind turbine blades: Influence of technology aspects. Wind Energy 2020;23:2247–55. http://dx.doi.org/10.1002/we.2552, URL: https://onlinelibrary.wiley.com/doi/abs/10.1002/we.2552.

[6] Frost-Jensen Johansen N. Test methods for evaluating rain erosion performance of wind turbine blade leading edge protection systems (Ph.D. thesis), Kgs. Lyngby: Technical University of Denmark; 2020, URL: https://orbit.dtu.dk/files/236330239/PHD_thesis_Nicolai_Frost_Jensen_Johansen.pdf.

[7] Fæster S, Johansen NF-J, Mishnaevsky Jr L, Kusano Y, Bech JI, Madsen MB. Rain erosion of wind turbine blades and the effect of air bubbles in the coatings. Wind Energy 2021;24:1071–82. http://dx.doi.org/10.1002/we.2617, URL: https://onlinelibrary.wiley.com/doi/abs/10.1002/we.2617.

[8] Bech JI, Johansen NF-J, Madsen MB, Hannesdóttir A, Hasager CB. Experimental study on the effect of drop size in rain erosion test and on lifetime prediction of wind turbine blades. Renew Energy 2022;197:776–89. http://dx.doi.org/10.1016/j.renene.2022.06.127, URL: https://www.sciencedirect.com/science/article/pii/S0960148122009673.

[9] Yang HM. 1.8 Aramid fibers. In: Beaumont PWR, Zweben CH, editors. Comprehensive composite materials II. Oxford: Elsevier; 2018, p. 187–217. http://dx.doi.org/10.1016/B978-0-12-803581-8.10303-0, URL: https://www.sciencedirect.com/science/article/pii/B9780128035818103030.

[10] Gore PM, Kandasubramanian B. Functionalized aramid fibers and composites for protective applications: A review. Ind Eng Chem Res 2018;57:16537–63. http://dx.doi.org/10.1021/acs.iecr.8b04903.

[11] Cheeseman BA, Bogetti TA. Ballistic impact into fabric and compliant composite laminates. Compos Struct 2003;61:161–73. http://dx.doi.org/10.1016/S0263-8223(03)00029-1, URL: https://linkinghub.elsevier.com/retrieve/pii/S0263822303000291.

[12] Giannopoulos IP, Burgoyne CJ. Stress limits for aramid fibres. Proc Inst Civ Eng - Struct Build 2009;162:221–32. http://dx.doi.org/10.1680/stbu.2009.162.4.221, URL: https://www.icevirtuallibrary.com/doi/10.1680/stbu.2009.162.4.221.

[13] Hinzmann C, Johansen NF-J, Hasager CB, Holst B. Towards greener wind power: nanodiamond-treated flax fiber composites outperform standard glass fiber composites in impact fatigue tests. Composites A 2024. under review.

[14] Ku H, Wang H, Pattarachaiyakoop N, Trada M. A review on the tensile properties of natural fiber reinforced polymer composites. Composites B 2011;42:856–73. http://dx.doi.org/10.1016/j.compositesb.2011.01.010, URL: https://www.sciencedirect.com/science/article/pii/S1359836811000382.

[15] Li M, Pu Y, Thomas VM, Yoo CG, Ozcan S, Deng Y, Nelson K, Ragauskas AJ. Recent advancements of plant-based natural fiber–reinforced composites and their applications. Composites B 2020;200:108254. http://dx.doi.org/10.1016/j.compositesb.2020.108254, URL: https://www.sciencedirect.com/science/article/pii/S1359836820333047.

[16] Hinzmann C, Parsons DF, Fiedler J, Zalieckas J, Holst B. Nanodiamond-treated flax: improving properties of natural fibers. Cellulose 2024;31:685–701. http://dx.doi.org/10.1007/s10570-023-05585-y.

[17] Mochalin VN, Shenderova O, Ho D, Gogotsi Y. The properties and applications of nanodiamonds. Nature Nanotechnol 2012;7:11–23. http://dx.doi.org/10.1038/nnano.2011.209.

[18] Shah DU, Schubel PJ, Clifford MJ. Can flax replace e-glass in structural composites? a small wind turbine blade case study. Composites B 2013;52:172–81. http://dx.doi.org/10.1016/j.compositesb.2013.04.027, URL: https://www.sciencedirect.com/science/article/pii/S1359836813001753.

[19] Gaertner E, Rinker J, Sethuraman L, Zahle F, Anderson B, Barter G, Abbas N, Meng F, Bortolotti P, Skrzypinski W, Scott G, Feil R, Bredmose H, Dykes K, Shields M, Allen C, Viselli A. Iea wind tcp task 37: Definition of the iea 15-megawatt offshore reference wind turbine. 2020.

[20] Mendoza JCM, Cardenas EEV, Perez AIM, Ledesma SL, Torres MV. Experimental study of temperature erosion tests on bidirectional coated and uncoated composites materials. Mater Res Express 2020;7:015338. http://dx.doi.org/10.1088/2053-1591/ab69c3.

[21] Duc F, Bourban PE, Månson JAE. The role of twist and crimp on the vibration behaviour of flax fibre composites. Compos Sci Technol 2014;102:94–9. http://dx.doi.org/10.1016/j.compscitech.2014.07.004, URL: https://www.sciencedirect.com/science/article/pii/S0266353814002346.

[22] Shah DU, Schubel PJ, Clifford MJ. Modelling the effect of yarn twist on the tensile strength of unidirectional plant fibre yarn composites. J Compos Mater 2013;47:425–36. http://dx.doi.org/10.1177/0021998312440737.

[23] Van de Velde K, Baetens E. Thermal and mechanical properties of flax fibres as potential composite reinforcement. Macromol Mater Eng 2001;286:342–9. http://dx.doi.org/10.1002/1439-2054(20010601)286:6<342::AID-MAME342>3.0.CO;2-P, URL: https://onlinelibrary.wiley.com/doi/abs/10.1002/1439-2054%2820010601%29286%3A6%3C342%3A%3AID-MAME342%3E3.0.CO%3B2-P.

[24] Madsen B, Andersen TL, Lilholt H. Volumetric composition: Fiber content and porosity. In: Handbook of green materials. Materials and energy, vol. 5, World Scientific; 2013, p. 137–53. http://dx.doi.org/10.1142/9789814566469_0056, URL: https://www.worldscientific.com/doi/abs/10.1142/9789814566469_0056.

[25] Rude TJ, Strait LH, Ruhala LA. Measurement of fiber density by helium pycnometry. J Compos Mater 2000;34:1948–58. http://dx.doi.org/10.1106/NUYP-PARA-RA5R-7NUE.

[26] Mehmood S, Madsen B. Properties and performance of flax yarn/thermoplastic polyester composites. J Reinf Plast Compos 2012;31:1746–57. http://dx.doi.org/10.1177/0731684412441686.

[27] DuPont. Kevlar®aramid fiber technical guide. 2017, URL: https://www.dupont.com/content/dam/dupont/amer/us/en/safety/public/documents/en/Kevlar_Technical_Guide_0319.pdf.

[28] Fraisse A, Bech JI, Borum KK, Fedorov V, Frost-Jensen Johansen N, McGugan M, Mishnaevsky L, Kusano Y. Impact fatigue damage of coated glass fibre reinforced polymer laminate. Renew Energy 2018;126:1102–12. http://dx.doi.org/10.1016/j.renene.2018.04.043, URL: https://www.sciencedirect.com/science/article/pii/S0960148118304518.

[29] Frost-Jensen Johansen N, Mishnaevsky L, Dashtkar A, Williams NA, Fæster S, Silvello A, Cano IG, Hadavinia H. Nanoengineered graphene-reinforced coating for leading edge protection of wind turbine blades. Coatings 2021;11:1104. http://dx.doi.org/10.3390/coatings11091104, URL: https://www.mdpi.com/2079-6412/11/9/1104.

[30] Slot HM, Gelinck ERM, Rentrop C, van der Heide E. Leading edge erosion of coated wind turbine blades: Review of coating life models. Renew Energy 2015;80:837–48. http://dx.doi.org/10.1016/j.renene.2015.02.036, URL: https://www.sciencedirect.com/science/article/pii/S0960148115001366.

[31] Richardson MOW, Wisheart MJ. Review of low-velocity impact properties of composite materials. Composites A 1996;27:1123–31. http://dx.doi.org/10.1016/1359-835X(96)00074-7, URL: https://www.sciencedirect.com/science/article/pii/1359835X96000747.

[32] Kempf M, Skrabala O, Altstädt V. Acoustic emission analysis for characterisation of damage mechanisms in fibre reinforced thermosetting polyurethane and epoxy. Composites B 2014;56:477–83. http://dx.doi.org/10.1016/j.compositesb.2013.08.080, URL: https://www.sciencedirect.com/science/article/pii/S1359836813005027.

[33] Bohmann T, Schlamp M, Ehrlich I. Acoustic emission of material damages in glass fibre-reinforced plastics. Composites B 2018;155:444–51. http://dx.doi.org/10.1016/j.compositesb.2018.09.018, URL: https://www.sciencedirect.com/science/article/pii/S1359836818312940.

[34] Almeida RSM, Magalhães MD, Karim MN, Tushtev K, Rezwan K. Identifying damage mechanisms of composites by acoustic emission and supervised machine learning. Mater Des 2023;227:111745. http://dx.doi.org/10.1016/j.matdes.2023.111745, URL: https://www.sciencedirect.com/science/article/pii/S0264127523001600.

[35] Ltd EC. Technical datasheet: El2 epoxy laminating resin. 2023, URL: https://media.easycomposites.co.uk/datasheets/EC-TDS-EL2-Epoxy-Laminating-Resin.pdf.

[36] Le Duigou A, Baley C. Coupled micromechanical analysis and life cycle assessment as an integrated tool for natural fibre composites development. J Clean Prod 2014;83:61–9. http://dx.doi.org/10.1016/j.jclepro.2014.07.027, URL: https://www.sciencedirect.com/science/article/pii/S095965261400732X.

[37] Williams OA, editor. Nanodiamond. The Royal Society of Chemistry; 2014, http://dx.doi.org/10.1039/9781849737616, URL: https://books.rsc.org/books/edited-volume/1046/Nanodiamond.

[38] Kaw AK. Mechanics of composite materials. 2nd ed.. Boca Raton: CRC Press; 2005, http://dx.doi.org/10.1201/9781420058291.

[39] Baley C, Kervoëlen A, Le Duigou A, Goudenhooft C, Bourmaud A. Is the low shear modulus of flax fibres an advantage for polymer reinforcement? Mater Lett 2016;185:534–6. http://dx.doi.org/10.1016/j.matlet.2016.09.067, URL: https://www.sciencedirect.com/science/article/pii/S0167577X16315300.

[40] Lamon F, Maragoni L, Carraro PA, Quaresimin M. Fatigue damage evolution in woven composites with different architectures. Int J Fatigue 2023;167:107365. http://dx.doi.org/10.1016/j.ijfatigue.2022.107365, URL: https://www.sciencedirect.com/science/article/pii/S0142112322006156.

[41] A. Materials. Properties: E-glass fibre. 2023, URL: https://www.azom.com/properties.aspx?ArticleID=764.

[42] Zhong Y, Tran LQN, Kureemun U, Lee HP. Prediction of the mechanical behavior of flax polypropylene composites based on multi-scale finite element analysis. J Mater Sci 2017;52:4957–67. http://dx.doi.org/10.1007/s10853-016-0733-7.

[43] Modniks J, Andersons J. Modeling elastic properties of short flax fiber-reinforced composites by orientation averaging. Comput Mater Sci 2010;50:595–9. http://dx.doi.org/10.1016/j.commatsci.2010.09.022, URL: https://www.sciencedirect.com/science/article/pii/S0927025610005264.

[44] Gohardani O. Impact of erosion testing aspects on current and future flight conditions. Prog Aerosp Sci 2011;47:280–303. http://dx.doi.org/10.1016/j.paerosci.2011.04.001, URL: https://www.sciencedirect.com/science/article/pii/S0376042111000315.

[45] Hui D, Dutta PK. A new concept of shock mitigation by impedance-graded materials. Composites B 2011;42:2181–4. http://dx.doi.org/10.1016/j.compositesb.2011.05.016, URL: https://www.sciencedirect.com/science/article/pii/S1359836811002344.

[46] Landau LD, Lifshitz EM, Sykes JB, Reid WH, Dill EH. Theory of elasticity: 7 of course of theoretical physics. Phys Today 1960;13:44–6. http://dx.doi.org/10.1063/1.3057037.

[47] Achenbach J. Wave propagation in elastic solids. Elsevier; 1973.

[48] Treviso A, Van Genechten B, Mundo D, Tournour M. Damping in composite materials: Properties and models. Composites B 2015;78:144–52. http://dx.doi.org/10.1016/j.compositesb.2015.03.081, URL: https://www.sciencedirect.com/science/article/pii/S1359836815002139.

[49] Penn L, Bystry F, Karp W, Lee S. Aramid/epoxy vs. graphite/epoxy: Origin of the difference in strength at the interface. In: Ishida H, Kumar G, editors. Molecular characterization of composite interfaces, polymer science and technology. Berlin, Heidelberg: Springer; 1985, p. 93–109. http://dx.doi.org/10.1007/978-3-662-29084-2_6.

[50] Agrawal S, Singh KK, Sarkar P. Impact damage on fibre-reinforced polymer matrix composite – a review. J Compos Mater 2014;48:317–32. http://dx.doi.org/10.1177/0021998312472217.

[51] Guoqi Z, Goldsmith W, Dharan CH. Penetration of laminated kevlar by projectiles—i. experimental investigation. Int J Solids Struct 1992;29:399–420. http://dx.doi.org/10.1016/0020-7683(92)90207-A, URL: https://www.sciencedirect.com/science/article/pii/002076839290207A.

[52] Sikarwar R, Velmurugan R, Madhu V. Experimental and analytical study of high velocity impact on kevlar/epoxy composite plates. Open Eng 2012;2:638–49. http://dx.doi.org/10.2478/s13531-012-0029-x, URL: https://www.degruyter.com/document/doi/10.2478/s13531-012-0029-x/html.

[53] Rodríguez Millán M, Moreno CE, Marco M, Santiuste C, Miguélez H. Numerical analysis of the ballistic behaviour of kevlar®composite under impact of double-nosed stepped cylindrical projectiles. J Reinf Plast Compos 2016;35:124–37. http://dx.doi.org/10.1177/0731684415608004.

[54] Miller GF, Pursey H, Bullard EC. On the partition of energy between elastic waves in a semi-infinite solid. Proc R Soc Lond Ser A 1955;233:55–69. http://dx.doi.org/10.1098/rspa.1955.0245, URL: https://royalsocietypublishing.org/doi/10.1098/rspa.1955.0245.

[55] Rahman MZ. Mechanical and damping performances of flax fibre composites – a review. Composites C 2021;4:100081. http://dx.doi.org/10.1016/j.jcomc.2020.100081, URL: https://www.sciencedirect.com/science/article/pii/S2666682020300815.

[56] Peijs T, van Vught RJM, Govaert LE. Mechanical properties of poly(vinyl alcohol) fibres and composites. Composites 1995;26:83–90. http://dx.doi.org/10.1016/0010-4361(95)90407-Q, URL: https://www.sciencedirect.com/science/article/pii/001043619590407Q.

[57] Bos HL, Van Den Oever MJA, Peters OCJJ. Tensile and compressive properties of flax fibres for natural fibre reinforced composites. J Mater Sci 2002;37:1683–92. http://dx.doi.org/10.1023/A:1014925621252.

[58] Duc F, Bourban PE, Plummer CJG, Månson JAE. Damping of thermoset and thermoplastic flax fibre composites. Composites A 2014;64:115–23. http://dx.doi.org/10.1016/j.compositesa.2014.04.016, URL: https://www.sciencedirect.com/science/article/pii/S1359835X14001183.

[59] Yang W, Li Y. Sound absorption performance of natural fibers and their composites. Sci China Technol Sci 2012;55:2278–83. http://dx.doi.org/10.1007/s11431-012-4943-1.